



ARTICLE

Computational Analysis of Heat and Mass Transfer in Magnetized Darcy-Forchheimer Hybrid Nanofluid Flow with Porous Medium and Slip Effects

Nosheen Fatima¹, Nabeela Kousar¹, Khalil Ur Rehman^{2,3,*} and Wasfi Shatanawi^{2,4,5}

¹Faculty of Basic and Applied Sciences, Department of Mathematics, Air University, PAF Complex E-9, Islamabad, 44000, Pakistan

²Department of Mathematics and Sciences, College of Humanities and Sciences, Prince Sultan University, Riyadh, 11586, Saudi Arabia

³Department of Mathematics, Air University, PAF Complex E-9, Islamabad, 44000, Pakistan

⁴Department of Medical Research, China Medical University Hospital, China Medical University, Taichung, 40402, Taiwan

⁵Department of Mathematics, Faculty of Science, The Hashemite University, P.O Box 330127, Zarqa, 13133, Jordan

*Corresponding Author: Khalil Ur Rehman. Email: kurrehman@psu.edu.sa

Received: 08 October 2022 Accepted: 03 April 2023 Published: 03 August 2023

ABSTRACT

A computational analysis of magnetized hybrid Darcy-Forchheimer nanofluid flow across a flat surface is presented in this work. For the study of heat and mass transfer aspects viscous dissipation, activation energy, Joule heating, thermal radiation, and heat generation effects are considered. The suspension of nanoparticles single-walled carbon nanotubes (SWCNTs) and multi-walled carbon nanotubes (MWCNTs) are created by hybrid nanofluids. However, single-walled carbon nanotubes (SWCNTs) produce nanofluids, with water acting as conventional fluid, respectively. Nonlinear partial differential equations (PDEs) that describe the ultimate flow are converted to nonlinear ordinary differential equations (ODEs) using appropriate similarity transformation. The ODEs are dealt with numerically by means of MATLAB's inbuilt routine function `bvp4c`. Velocity, temperature, and concentration profiles are explained pictorially whereas Sherwood number, local skin friction coefficient, and Nusselt number values are represented through bar charts. Thermal radiation and activation parameters shows direct impact on flow field. Furthermore, hybrid nanofluid admits a higher magnitude of velocity and temperature than nanofluid, but the concentration profile exhibits the opposite trend. The notable findings of the present investigation have significant applications in heat combustion and cooling chambers, space technology, the ceramics industry, paint and conductive coatings, bio-sensors, and many more.

KEYWORDS

Heat transfer; hybrid nanofluid; MCNTs; SCNTs; MHD; Darcy-Forchheimer; joule heating; activation energy

1 Introduction

Nanofluids are created when simple nanoparticles are disseminated in basic fluids like oil, ethylene glycol, and water. Compared to regular liquids, these fluids have a higher thermal conductivity. Choi and Eastman [1] were the first to conduct a nanoparticle study at Argonne National Laboratory in



1995. They indicated that the nanofluid is made up of solid nanoparticles that are dispersed in the base fluid. Applications of nanofluids are microelectronics, hybrid-powered engines, pharmaceutical procedures, particle storage facilities, chemical catalytic reactors, electronic equipment cooling, and medicine diffusion in blood veins. Recently, scientists have focused their research on nanofluids to improve heat transfer fluids. Ibrahim and Shankar [2] examined the influence of MHD and heat radiation with slip boundary conditions over permeable stretched sheets using nanofluid. The shooting method combined with the fourth-order Runge–Kutta approach was used in solving higher-order ODEs numerically. Outcomes of concentration, velocity, and temperature distributions against various parameters were displayed numerically. They showed that when thermophoresis and Brownian motion parameters rise, then the Nusselt number falls whereas the Sherwood number becomes grows by raising the Brownian motion parameter. Maraj et al. [3] studied carbon nanotubes gravity-driven flow through vertical stretching surface. MHD effects are incorporated along the active and passive control models to calculate heat and mass transfer. To solve ODEs, the shooting approach was applied with the Runge Kutta Fehlberg method. The consequences of the velocity profile, temperature profile, rate of heat transfer, and coefficient of skin friction for various fluid flow parameters were explained using graphs and tables. They concluded that thermal radiation impacts drop fluid temperature while opposite behavior against Biot number. Hybrid nanofluids (HNFs) are an advanced category of nanofluids. HNFs are suspended into two distinct types of nanoparticles with diameters of less than 100 nanometers with conventional fluids like water. The thermal conductivity and thermo-physical parameters of this new type of nanofluid are greater than those of conventional fluids. Hybrid nanofluids have numerous heat transfer applications, including heat pipes, solar energy, heat exchangers, biomedical, spacecraft, coolant in machining and manufacturing, biomedical, ventilation, and air conditioning systems, to mention a few. Metals (e.g., Ag/silver, Cu/copper), Metal oxides (e.g., Al_2O_3 /alumina, CuO /cupric oxide, Fe_2O_3 /hematite, Fe_3O_4 /magnetite), carbon substances (e.g., CNTs/carbon nanotubes, graphite, and MWCNTs/multi-walled carbon nanotubes) these nanoparticles combined then formed HNFs. Rekha et al. [4] examined hybrid nanofluid flow in cone, wedge, and plate using an aluminum alloy dispersion as a nanoparticle in base fluid water with the influence of heat sink and source. Shooting approach was used for solving governing equations using RKF-45. The behavior of velocity, concentration, and temperature profiles was depicted using graphs. When compared to a cone or wedge, fluid flow over a plate exhibits a higher heat transfer rate by raising heat source and sink parameter values.

Carbon nanotubes (CNTs) have a cylindrical shape and are made up of carbon atoms. CNTs are classified into three categories based on graphene layers: single-walled CNTs (SWCNTs) with 0.5 to 1.5 nm diameter, double-walled CNTs (DWCNTs), and multi-walled CNTs (MWCNTs), with 10 to 100 nm diameter. Hardness, adhesion, high mechanical strength, stiffness, chemical steadiness, great thermal and electrical conductivity, biological and chemical sensors, nanotechnology, catalysis, conductive polymers, and structural composite materials are just a few applications of hybrid nanofluids. Carbon nanotube suspensions have better thermal conductivity than the same volume fraction of other nanoparticles, according to references [5,6]. Shanmugapriya et al. [7] examined the moving wedge by taking the effects of MHD, heat radiation, and activation energy for two types of hybrid nanoparticles, SWCNTs and MWCNTs. The equations were numerically solved by utilizing the shooting approach in association with RKF 4-5th order. Graphs and tables were used to represent the findings. They reached the conclusion that heat transfer in a hybrid nanofluid has a greater impact

than in a common fluid. Several scientists have recently studied the exact and numerical solutions for heat and mass transfer flow over various geometries, as indicated in [8–12].

Porous media is a porous material that has pores that are usually filled with fluid. There are numerous applications related to porous media, including paper manufacture, nonwoven materials, electrical technology, energy storage, heat pipe technology. Darcy's law does not apply at greater rate of flow because of inertial and boundary effects. To circumvent this limitation, in 1901 a Dutch scientist, Philippe Forchheimer, modified that by predicting the flow of inertia and the flow of the boundary layer, Darcian velocity expression was changed by introducing the square velocity term to momentum equation [13]. Firstly, Muskat [14] invented the term "Forchheimer factor" to express this unique idea. Sajid et al. [15] analyzed a linearly stretching surface with Darcy-Forchheimer by considering Maxwell nanofluid flow. They added the assumptions like thermal radiation, activation energy, variable thermal conductivity, convective boundary conditions, and zero mass flux. They concluded that thermophoresis and activation energy parameter had an increasing influence on the concentration profile. Khan et al. [16] observed a hybrid nanofluid (MoS_2, SiO_2) via a stretching surface with entropy generation, heat exchange, and Darcy-Forchheimer flow. Outcomes indicated that when the porosity parameter rises the temperature of fluid decrease. Some latest studies related to Darcy-Forchheimer are found in [17–22].

The least amount of energy required to initiate a chemical reaction is known as activation energy. The Arrhenius equation describes the change in rate constants with temperature and is used to determine activation energy. In the mass transfer equation, activation energy is combined with binary chemical reactions that have various uses in food processing, oil reservoirs, water and oil suspensions, chemical and geothermal engineering, and other disciplines. Bestman [23] was the first to introduce this concept. Khan et al. [24] researched Casson nanofluid flow across a stretching sheet by accounting for the effects of activation energy, thermal radiation, heat sink/source, and entropy generation. Under these effects, they formulated the governing equations and solved them numerically using bvp4c technique. Graphical representations were utilized to depict the various flow parameters affected by the profiles of velocity, temperature, concentration, and entropy generation. They noticed that the concentration profile decreases against higher values of the activation energy parameter. Activation energy impact on hybrid nanofluids under various circumstances was identified by a group of scientists, see [25–28].

According to the literature review, the main purpose of this study is to investigate MHD stagnation point flow through a porous medium with mixed convection across a permeable stretched sheet. For a more realistic study, the Darcy-Forchheimer approach has been incorporated. Moreover, the effect of Joule heating due to the external magnetic field is also explored with existence of viscous dissipation, thermal radiation, and heat generation phenomena. Furthermore, solute concentration is also examined under the influence of activation energy and concentration slip at the surface. This study is essentially a comparison of hybrid nanofluids (MWCNTs-SWCNTs/water) and nanofluid (SWCNTs/water) with concentration, thermal, and momentum boundary layer. To the best of the author's knowledge no such attempt is mentioned in literature. The novel findings for the present investigation may impart noteworthy contributions to the hybrid CNTs as coolants in mechanical procedures and space technology, conductive coating, the polymer industry, and so forth.

2 Mathematical Formulation

We are considering laminar, two-dimensional, steady, and incompressible stagnation point flow for electrically conducting hybrid nanofluid and nanofluid above a porous stretching sheet, with

impacts: viscosity dissipation, joule heating, and velocity slip. This study also involves these effects activation energy, heat generation, nonlinearly variable thermal radiation, concentration slip, Soret effect, and uniformly heated boundary condition. Fluid flows in x -direction along with the sheet while it flows perpendicular to it in y -direction. The strength of magnetic field B_0 is applied externally in a perpendicular direction. Furthermore, surface temperature and concentration are taken as $T_w = T_\infty + Ax^2/L^2$ and $C_w = C_\infty + Bx^2/L^2$. Moreover, stretching sheet velocity is considered to be $u_w = bx$. $U_e = ax$, T_∞ , and C_∞ are the free stream velocity, ambient temperature, and ambient concentration, respectively, where a and b are positive constants. CNTs with single and multiple walls are uniformly distributed with base fluid. Fig. 1 depicts and describes the physical geometry of the problem.

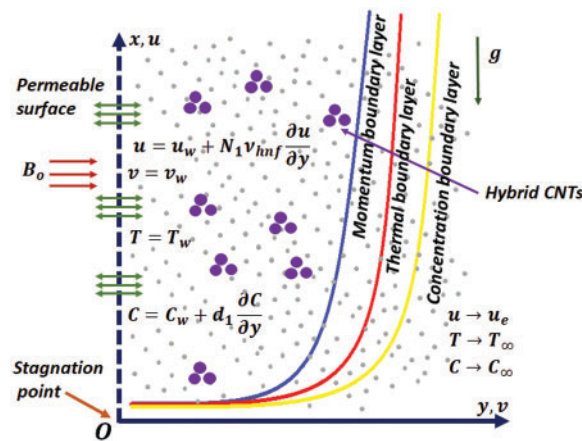


Figure 1: Physical configuration of the current model

Table 1 demonstrates the thermo-physical properties of nanoparticles and base fluid. Table 2 displays thermo-physical properties of single and multi-walled CNTs with base fluid H_2O after the following models are recommended by Maxwell [29], Brinkman [30], and Xuan et al. [31]. In Table 2, ϕ_1 indicates volume fraction for MWCNTs nanoparticle, whereas ϕ_2 represents volume fraction for SWCNTs nanoparticle. The subscripts $h1$ and $h2$ denote MWCNTs and SWCNTs, respectively.

Table 1: Thermo-physical properties of base fluid and CNTs nanoparticles [32]

Physical properties	Base fluid H_2O	CNTs nanoparticles	
		SWCNTs	MWCNTs
$k(W/mK)$	0.613	6600	3000
$\rho(kg/m^3)$	997.1	2600	1600
$c_p(J/kgK)$	4179	425	796
$\beta(K^{-1})$	21	27	44
$\sigma(\Omega^{-1}m^{-1})$	5.5×10^{-6}	10^6	1.9^{-4}

Table 2: Thermo-physical properties of hybrid nanofluid

Properties	Hybrid nanofluid
Viscosity	$\frac{\mu_{hnf}}{\mu_f} = \frac{1}{(1 - \phi_1)^{2.5}(1 - \phi_2)^{2.5}}$
Density	$\frac{\rho_{hnf}}{\rho_f} = (1 - \phi_2) \left[(1 - \phi_1) + \phi_1 \frac{\rho_{h1}}{\rho_f} \right] + \phi_2 \frac{\rho_{h2}}{\rho_f}$
Electrical conductivity	$\frac{\sigma_{hnf}}{\sigma_f} = \left(1 + \frac{3\phi_1 \left(\frac{\sigma_{h1}}{\sigma_f} - 1 \right)}{\left(\frac{\sigma_{h1}}{\sigma_f} + 2 \right) - \phi_1 \left(\frac{\sigma_{h1}}{\sigma_f} - 1 \right)} \right) \times \left(1 + \frac{3\phi_2 \left(\frac{\sigma_{h2}}{\sigma_f} - 1 \right)}{\left(\frac{\sigma_{h2}}{\sigma_f} + 2 \right) - \phi_2 \left(\frac{\sigma_{h2}}{\sigma_f} - 1 \right)} \right)$
Thermal expansion	$\frac{(\rho\beta)_{hnf}}{(\rho\beta)_f} = (1 - \phi_2) \left[(1 - \phi_1) + \phi_1 \frac{(\rho\beta)_{h1}}{(\rho\beta)_f} \right] + \phi_2 \frac{(\rho\beta)_{h2}}{(\rho\beta)_f}$
Thermal conductivity	$\frac{k_{hnf}}{k_f} = \left(\frac{1 - \phi_1 + 2\phi_1 \frac{k_{h1}}{k_{h1} - k_f} \ln \left(\frac{k_{h1} + k_f}{2k_f} \right)}{1 - \phi_1 + 2\phi_1 \frac{k_f}{k_{h1} - k_f} \ln \left(\frac{k_{h1} + k_f}{2k_f} \right)} \right) \times \left(\frac{1 - \phi_2 + 2\phi_2 \frac{k_{h2}}{k_{h2} - k_f} \ln \left(\frac{k_{h2} + k_f}{2k_f} \right)}{1 - \phi_2 + 2\phi_2 \frac{k_f}{k_{h2} - k_f} \ln \left(\frac{k_{h2} + k_f}{2k_f} \right)} \right)$
Heat capacitance	$\frac{(\rho c_p)_{hnf}}{(\rho c_p)_f} = (1 - \phi_2) \left[(1 - \phi_1) + \phi_1 \frac{(\rho c_p)_{h1}}{(\rho c_p)_f} \right] + \phi_2 \frac{(\rho c_p)_{h2}}{(\rho c_p)_f}$

The governing system of equations based on boundary layer approximation theory is followed by:

$$u \frac{\partial u}{\partial x} + v \frac{\partial v}{\partial y} = 0 \tag{1}$$

$$u \frac{\partial u}{\partial x} + v \frac{\partial u}{\partial y} = U_e \frac{dU_e}{dx} + \frac{\mu_{hnf}}{\rho_{hnf}} \frac{\partial^2 u}{\partial y^2} - \frac{\sigma_{hnf} B_0^2}{\rho_{hnf}} (u - U_e) - \frac{\mu_{hnf}}{\rho_{hnf}} \frac{1}{K_0} (u - U_e) - \frac{F}{\rho_{hnf}} (u - U_e)^2 + \frac{g(\rho\beta_T)_{hnf} (T - T_\infty)}{\rho_{hnf}} + \frac{g(\rho\beta_C)_{hnf} (C - C_\infty)}{\rho_{hnf}}, \tag{2}$$

$$u \frac{\partial T}{\partial x} + v \frac{\partial T}{\partial y} = \frac{k_{hnf}}{(\rho c_p)_{hnf}} \frac{\partial^2 T}{\partial y^2} + \frac{\mu_{hnf}}{(\rho c_p)_{hnf}} \left(\frac{\partial u}{\partial y} \right)^2 + \frac{\sigma_{hnf} B_0^2 u^2}{(\rho c_p)_{hnf}} - \frac{1}{(\rho c_p)_{hnf}} \frac{\partial q_r}{\partial y} + \frac{Q_0 (T - T_\infty)}{(\rho c_p)_{hnf}}, \tag{3}$$

$$u \frac{\partial C}{\partial x} + v \frac{\partial C}{\partial y} = D_m \frac{\partial^2 C}{\partial y^2} + D_t \frac{\partial^2 T}{\partial y^2} - \Lambda^2 (C - C_\infty) \left(\frac{T}{T_\infty} \right)^n \text{Exp} \left(-\frac{E_a}{k_1 T} \right), \quad (4)$$

and related boundary conditions are:

$$u = u_w + N_1 \frac{\mu_{hnf}}{\rho_{hnf}} \frac{\partial u}{\partial y}, \quad v = v_w, \quad T = T_w, \quad C = C_w + d_1 \frac{\partial C}{\partial y} \quad \text{at} \quad y = 0, \quad (5)$$

$$u \rightarrow U_e, \quad T \rightarrow T_\infty, \quad C \rightarrow C_\infty \quad \text{as} \quad y \rightarrow \infty,$$

where, u and v are horizontal and vertical velocity components, respectively. Subscript hnf stands for hybrid nanofluid and symbols $\mu, \rho, \sigma, K_0, B_0 F, g, k, q_r, Q_0, D_m, D_t, \Lambda, n, E_a, k_1, N_1, d_1,$ and $(T/T_\infty)^n \text{Exp}(-E_a/k_1 T)$ represents dynamic viscosity, density, electric conductivity, the permeability of the porous medium, magnetic field strength, nonlinear inertia coefficient of the porous space, gravitational acceleration, thermal conductivity, radiative heat flux, heat generation coefficient, mass diffusivity, thermo-diffusion coefficient, chemical reaction rate, fitted rate constants, activation energy, Boltzmann constant, velocity and concentration slip coefficients, and modified Arrhenius function, respectively.

The Rosseland approximation for thermal radiation is implemented to compute radiative heat flux q_r [33,34].

$$q_r = -\frac{4\sigma^*}{3k^*} \frac{\partial T^4}{\partial y}, \quad (6)$$

T^4 expands in Taylor series as $T^4 = 4T_\infty^3 T - 3\sigma T_\infty^4$, so

$$q_r = -\frac{16\sigma^* T_\infty^3}{3k^*} \frac{\partial T}{\partial y}, \quad (7)$$

here σ^* and k^* stand for Stefan Boltzmann constant and Rosseland mean absorption coefficient. Using Eqs. (7) and (3) is written as:

$$u \frac{\partial T}{\partial x} + v \frac{\partial T}{\partial y} = \frac{k_{hnf}}{(\rho c_p)_{hnf}} \frac{\partial^2 T}{\partial y^2} + \frac{\mu_{hnf}}{(\rho c_p)_{hnf}} \left(\frac{\partial u}{\partial y} \right)^2 + \frac{\sigma_{hnf} B_o^2 u^2}{(\rho c_p)_{hnf}} - \frac{16}{3} \frac{\sigma^* T_\infty^3}{k^* (\rho c_p)_{hnf}} \frac{\partial^2 T}{\partial y^2} + \frac{Q_0 (T - T_\infty)}{(\rho c_p)_{hnf}}. \quad (8)$$

By invoking following similarity variables (according to [34]).

$$\eta = y \sqrt{\frac{u_w}{v_f x}}, \quad u = u_w f'(\eta), \quad v = -\sqrt{\frac{u_w v_f}{x}} f(\eta), \quad \theta(\eta) = \frac{T - T_\infty}{T_w - T_\infty}, \quad \alpha(\eta) = \frac{C - C_\infty}{C_w - C_\infty}. \quad (9)$$

Here prime means differentiation with respect to η . Continuity equation in Eq. (1) is satisfied whereas Eqs. (2), (4) and (8) simplifies as:

$$f''' + \frac{A_2}{A_1} (ff'' - f'^2 + \lambda^2) - \left(\frac{A_3}{A_1} M + K \right) (f' - \lambda) - \frac{1}{A_1} Fr (f' - \lambda)^2 + \frac{A_4}{A_1} (Gr\theta + Gc\alpha) = 0, \quad (10)$$

$$[A_5 + N((\theta_r - 1)\theta + 1)^3] \theta'' - A_6 Pr (2f'\theta - f\theta') + A_1 Ec Pr f''^2 + A_3 M Ec Pr f'^2 + Q Pr \theta = 0, \quad (11)$$

$$\alpha'' - Sc \left(2f'\alpha - f\alpha' - Sr\theta'' + Kr\alpha((\theta_r - 1)\theta + 1)^n \text{Exp} \left(-\frac{E}{(\theta_r - 1)\theta + 1} \right) \right) = 0, \quad (12)$$

and boundary conditions in Eq. (5) are converted into Eq. (13).

$$f(\eta) = V, f'(\eta) = 1 + \frac{A_1}{A_2} \delta f''(\eta), \theta(\eta) = 1, \alpha(\eta) = 1 + \delta_1 \alpha'(\eta) \quad \text{at} \quad \eta = 0 \tag{13}$$

$$f'(\eta) \rightarrow \lambda, \theta(\eta) \rightarrow 0, \alpha(\eta) \rightarrow 0 \quad \text{as} \quad \eta \rightarrow \infty$$

where

$$A_1 = \frac{\mu_{hnf}}{\mu_f}, A_2 = \frac{\rho_{hnf}}{\rho_f}, A_3 = \frac{\sigma_{hnf}}{\sigma_f}, A_4 = \frac{(\rho\beta)_{hnf}}{(\rho\beta)_f}, A_5 = \frac{k_{hnf}}{k_f}, A_6 = \frac{(\rho c_p)_{hnf}}{(\rho c_p)_f}. \tag{14}$$

The non-dimensional parameters are the velocity ratio parameter $\lambda = \frac{a}{b}$, Hartmann number $M = \frac{B_o^2 \sigma_f}{b \rho_f}$, porosity parameter $K = \frac{v_f}{b K_0}$, Forchheimer number $Fr = \frac{F}{\rho_f} x$, temperature Grashof number $Gr = \frac{g(\rho\beta)_f(T_w - T_\infty)}{U_w^2 \rho_f}$, concentration Grashof number $Gc = \frac{g(\rho\beta)_f(C_w - C_\infty)}{U_w^2 \rho_f}$, Eckert number $Ec = \frac{L^2 b^2}{A(c_p)_f}$, Prandtl number $Pr = \frac{v_f(\rho c_p)_f}{k_f}$, thermal radiation parameter $N = \frac{16 \sigma^* T_\infty^3}{3 k^* k_f}$, temperature ratio variable $\theta_r = \frac{T_w}{T_\infty}$, heat generation parameter $Q = \frac{Q_0(\rho c_p)_f}{b}$, Schmidt number $Sc = \frac{v_f}{D_m}$, activation energy parameter $E = \frac{E_a}{k_1 T_\infty}$, chemical reaction parameter $Kr = \frac{\Lambda^2}{b}$, Soret number $Sr = \frac{D_r A}{D_m B}$, velocity slip parameter $\delta = N_1 \sqrt{b v_f}$, suction parameter $V = -\frac{v_w}{\sqrt{b v_f}}$, and concentration slip parameter $\delta_1 = d_1 \sqrt{\frac{b}{v_f}}$.

For an engineering perspective, the local skin friction coefficient C_{fx} , Nusselt number Nu_x , and Sherwood number Sh_x are essential physical variables, are stated as:

$$C_{fx} = \frac{2\tau_w}{\rho_f u_w^2}, \quad Nu_x = \frac{x q_w}{k_f(T_w - T_\infty)}, \quad Sh_x = \frac{x j_w}{D_m(C_w - C_\infty)}, \tag{15}$$

where

$$\tau_w = \mu_{hnf} \left(\frac{\partial u}{\partial y} \right)_{y=0}, \quad q_w = -k_{hnf} \left(\frac{\partial T}{\partial y} \right)_{y=0} + (q_r)_{y=0} = - \left(k_{hnf} + \frac{16\sigma^* T_\infty^3}{3k^*} \right) \left(\frac{\partial T}{\partial y} \right)_{y=0}, \tag{16}$$

$$j_w = -D_m \left(\frac{\partial C}{\partial y} \right)_{y=0}.$$

By invoking Eq. (9), the expressions defined in Eq. (16) take the following form:

$$C_f \sqrt{Re_x} = 2A_1 f''(0), \frac{Nu_x}{\sqrt{Re_x}} = - (A_5 + N((\theta_r - 1)\theta(0) + 1)^3) \theta'(0), \frac{Sh_x}{\sqrt{Re_x}} = -\phi'(0), \tag{17}$$

where $Re_x = \frac{u_w x}{v_f}$ stands for local Reynolds number.

3 Solution Methodology

Nonlinear ODEs are written in Eqs. (10)–(12) and their boundary conditions in Eq. (13) are tackled with the `bvp4c` function in MATLAB numerically. The finite difference approach is used by the `bvp4c` solver to implement three steps of the Lobatto IIIa formula. The procedure of the `bvp4c` technique is listed in Fig. 2. To begin the `bvp4c` method. We should first convert Eqs. (10)–(12) into first-order ODEs. We suggest different parameters for this purpose:

$$y_1 = f, \quad y_2 = f', \quad y_3 = f'', \quad y_4 = \theta, \quad y_5 = \theta', \quad y_6 = \alpha, \quad y_7 = \alpha', \tag{18}$$

by inserting Eq. (18) into Eqs. (10)–(12), we get

$$\begin{aligned} y_1' &= y_2, \\ y_2' &= y_3, \\ y_3' &= -\frac{A_2}{A_1}(y_1 y_3 - y_2^2 + \lambda^2) + \left(\frac{A_3}{A_1}M + K\right)(y_2 - \lambda) + \frac{Fr}{A_1}(y_2 - \lambda)^2 - \frac{A_4}{A_1}(Gr y_4 + Gc y_6), \\ y_4' &= y_5, \end{aligned} \tag{19}$$

$$y_5' = \frac{Pr}{(A_5 + N((\theta_r - 1)y_4 + 1)^3)} (A_6(2y_2 y_4 - y_1 y_5) - A_1 Ec y_3^2 - A_3 M Ec y_2^2 - Q y_4),$$

$$y_6' = y_7,$$

$$y_7' = Sc \left(2y_2 \alpha - y_1 y_7 - Sr y_5' + Kr y_6 ((\theta_r - 1)y_4 + 1)^n \exp\left(-\frac{E}{(\theta_r - 1)y_4 + 1}\right) \right),$$

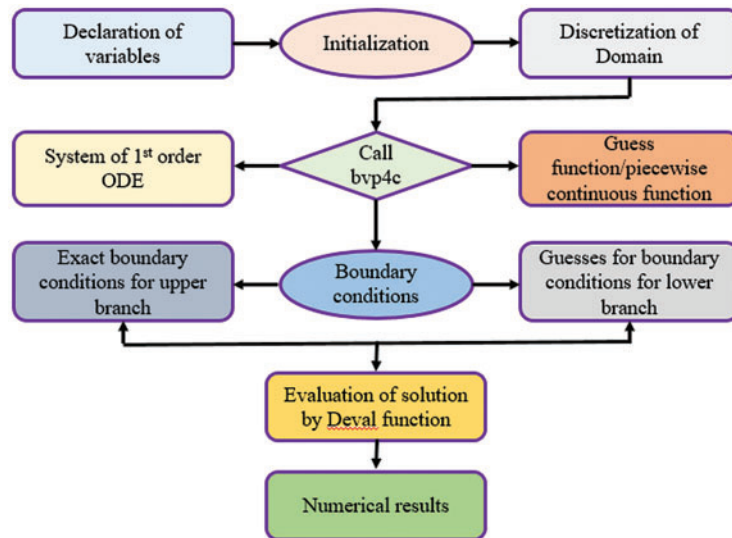


Figure 2: Phases for scheme `bvp4c`

Using Eq. (18), the boundary conditions given in Eq. (13) are as follows:

$$\begin{aligned} \eta = 0 : \quad & y_1(0) = V, \quad y_2(0) = 1 + \frac{A_1}{A_2} \delta y_3(0), \quad y_4(0) = 1, \quad y_6(0) = 1 + \delta_1 y_7(0), \\ \eta \rightarrow \infty : \quad & y_2(\infty) \rightarrow \lambda, \quad y_4(\infty) \rightarrow 0, \quad y_6(\infty) \rightarrow 0. \end{aligned} \tag{20}$$

We calculated skin friction coefficient values for varying the velocity slip parameter δ to verify the accuracy and correctness of the resulting solution by taking $\phi_1 = \phi_2 = M = \lambda = K = Fr = Gr =$

$Gc = 0$. We compared our outcomes with those published results as Wang [35], Noghrehabadi et al. [36] and Nandi et al. [34], see Table 3. The comparison illustrations that current outcomes are in excellent agreement with published outcomes.

Table 3: Comparison $C_f\sqrt{Re_x}/2$ for different values of δ

δ	Wang [35]	Noghrehabadi et al. [36]	Nandi et al. [34]	Current outcome
0.0	1.0	1.0000	1.0000	1.0005
1.0	0.430	0.4302	0.4301	0.4311
2.0	0.284	0.2839	0.2840	0.2847
5.0	0.145	0.1449	0.1449	0.1452
20.0	0.0438	0.0438	0.0438	0.0440

Table 4 represents the grid independence test for various values of tolerance by setting $\phi_1 = 0.01$, $\phi_2 = 0.02$, $M = 0.5$, $\lambda = 0.1$, $K = 6$, $Fr = 2$, $Gr = 2.5$, $Gc = 1.5$, $V = 0.1$, $\delta = 2$, $Pr = 7.2$, $\theta_r = 1.6$, $Ec = 0.1$, $Q = 0.1$, $n = N = 2$, $\delta_1 = 0.8$, $Sc = 6$, $Sr = 0.3$, $Kr = 0.5$, $E = 3$ these parameter values. Skin friction, Nusselt number, and Sherwood number values are seen for exhibit convergent behavior via declining tolerance.

Table 4: Grid independence test for $C_f\sqrt{Re_x}$, $Nu_x/\sqrt{Re_x}$ and $Sh_x/\sqrt{Re_x}$

ξ	$C_f\sqrt{Re_x}$	$Nu_x/\sqrt{Re_x}$	$Sh_x/\sqrt{Re_x}$
10^{-2}	-0.516881253309542	10.409466515074003	0.570914610200291
10^{-3}	-0.516881253309542	10.409466515074003	0.570914610200291
10^{-4}	-0.516881253309542	10.409466515074003	0.570914610200291
10^{-5}	-0.516881253309542	10.409466515074003	0.570914610200291
10^{-6}	-0.516881271555508	10.409467955257171	0.570914584681199

4 Outcomes and Discussion

We examine the heat and mass properties of both nanofluid and hybrid nanofluid in this article. Multi-walled carbon nanotubes (MWCNTs) have volume fraction ϕ_1 and single-walled carbon nanotubes (SWCNTs) have volume fraction ϕ_2 . We are considering $\phi_1 = 0$ and $\phi_2 = 0.02$ for nanofluid (SWCNTs-water) and $\phi_1 = 0.01$ and $\phi_2 = 0.02$ for hybrid nanofluids (SWCNTs-MWCNTs/water) throughout the analysis. Influences of various parameters on the profiles of velocity, temperature, and concentration are evaluated through graphical observations. The effect of some developing parameters for velocity field is shown in Figs. 3a–3i. The volume fraction ϕ_2 effect on velocity field, see Fig. 3a. The velocity distribution enhances by rising nanoparticle volume fraction ϕ_2 and reported that hybrid nanofluid achieves advanced velocity than nanofluid. This indicates that the existence of nanoparticles leads to fall in viscosity and therefore resistance to the fluid flow declines. Fig. 3b illustrates velocity ratio parameter λ influence on velocity field. Velocity of free stream exceeds then stretching velocity as λ is increased so enhancing velocity profile. For $\lambda = 1$ ($a = b$), no boundary layer exists due to identical velocity of the sheet and fluid. For $\lambda > 1$, velocity of free stream exceeds the velocity of stretching sheet then velocity upsurges and the boundary layer thickness falls. Additionally, velocity

and boundary layer thickness both drop when the free stream velocity is smaller than the stretching velocity for $\lambda < 1$. Moreover, velocity of nanofluid is higher than hybrid nanofluid for $\lambda \geq 1$ but a contrary trend is noted for $\lambda < 1$. Fig. 3c displays Hartmann number M influence on velocity profile. The velocity profile reduces as raising M . This is because, M represents the contribution of Lorentz force, an increase in M indicates enhanced Lorentz force which offers more resistance to fluid transport and, subsequently fluid velocity decrease. Moreover, in comparison to nanofluid, hybrid nanofluid has a larger magnitude. The sway of Forchheimer number on velocity distribution is presented in Fig. 3d. The velocity of fluid decreases as Fr raises, however, nanofluid has lower velocity than hybrid nanofluid. The cause of this trend is the fact that Fr is the ratio of nonlinear drag coefficient of porous medium to fluid density and thus, an increase in Fr indicates an increase in drag coefficient with enhances resistance to fluid flow. Fig. 3e illustrates the porosity parameter K impact on the velocity profile. For raising K the influence on velocity profile is reduced. This is because when K grows, then matrix of the porous media becomes denser, increasing flow resistance and causing a reduction in velocity field. Furthermore, hybrid nanofluids (SWCNTs-MWCNTs/water) have a higher velocity than nanofluids (SWCNTs-water). Fig. 3f portrays the thermal Grashof number Gr impact on velocity profile. This graph shows that rising value of Gr results in upsurges in fluid velocity as well. This is due to Gr links with both hydrodynamic force and thermal buoyancy force that happens on boundary layer, because of changes in temperature. As a result, thermal buoyancy effect of fluid rises, enabling the specified liquid to cool the uniformly heated plate. Furthermore, the velocity of nanofluid is found to be lower than that of hybrid nanofluid. Concentration Grashof number Gc sway on velocity field is shown in Fig. 3g. Velocity profile upsurges as increasing Gc (mass convective/species buoyancy). This behavior developed due to the influence of the buoyancy force of the riding species, which helps to raise boundary layer thickness farther from the sheet. Furthermore, hybrid nanofluid (SWCNTs-MWCNTs/water) has a greater velocity than nanofluid (SWCNTs-water). Fig. 3h demonstrates the suction parameter V influence on velocity distribution. Suction is used to tackle hybrid nanofluid and nanofluid flow, because it reduces the drag on nanoparticles in an external flow, therefore, lowering velocity. Additionally, hybrid nanofluid has a higher velocity than nanofluid. Fig. 3i shows the sway of velocity slip parameter δ on $f'(\eta)$. As δ increasing, velocity of hybrid nanofluid and nanofluid is decreases. Physically, slip rises as the value δ increases, therefore the velocity of permeable stretching sheet transferred to fluid is worse than for the case of no-slip. Moreover, in comparison, the magnitude of velocity for nanofluid is less than the hybrid nanofluid.

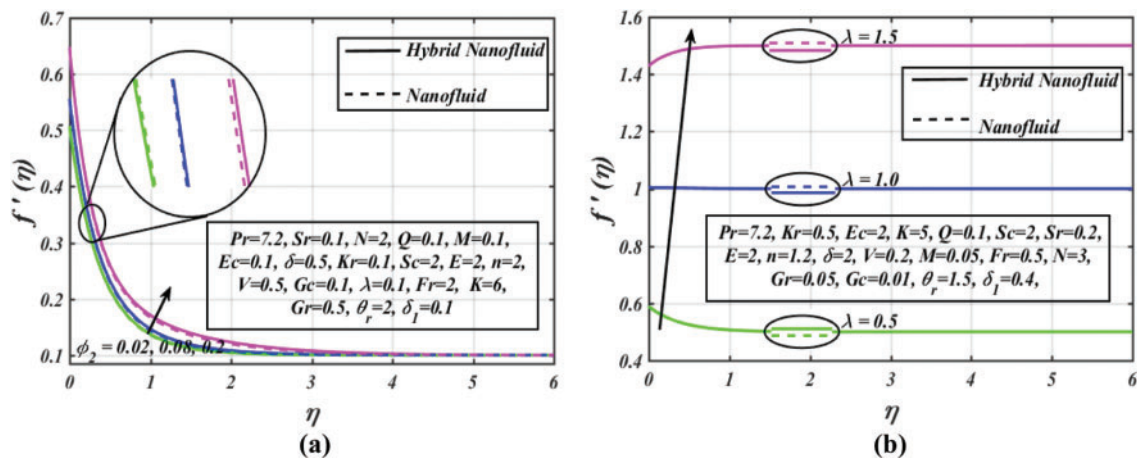


Figure 3: (Continued)

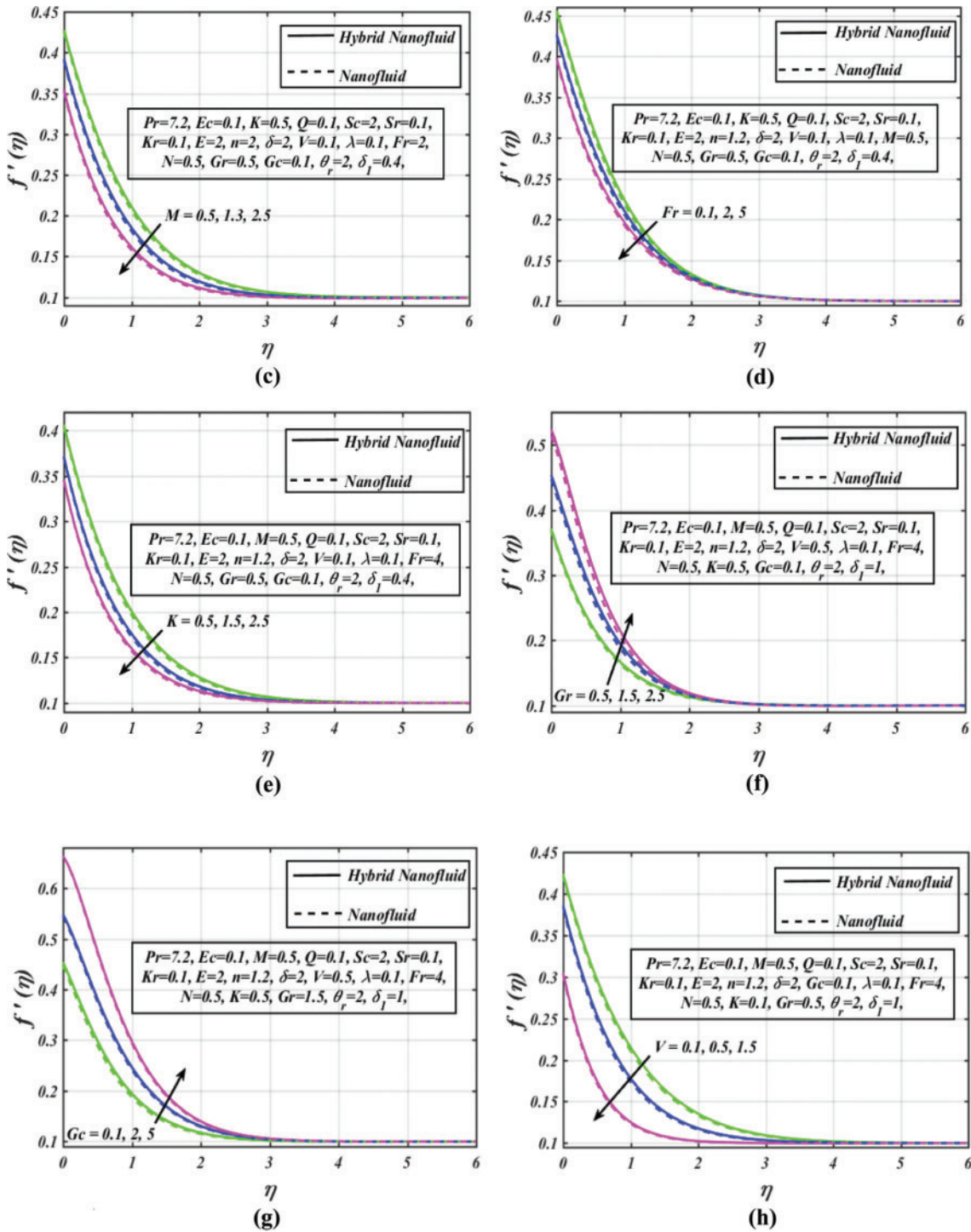


Figure 3: (Continued)

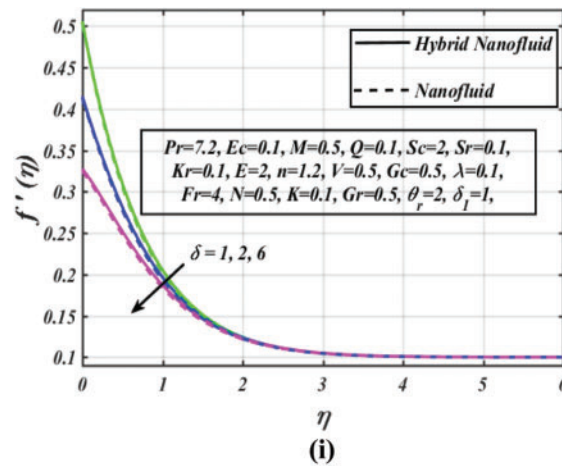


Figure 3: (a) Velocity profile vs. several ϕ_2 values. (b) Velocity profile vs. several λ values. (c) Velocity profile vs. several M values. (d) Velocity profile vs. several Fr values. (e) Velocity profile vs. several K values. (f) Velocity profile vs. several Gr values. (g) Velocity profile vs. several Gc values. (h) Velocity profile vs. several V values. (i) Velocity profile vs. several δ values

Figs. 4a–4f show a series of graphs that assist us to visualize the variations in temperature profiles induced by various prominent parameters. Fig. 4a provides sway of nanoparticles volume fraction ϕ_2 on the temperature profile. Temperature profile enhances by raising volume fraction ϕ_2 but the temperature of nanofluid has lower than hybrid nanofluid. Because volume fractions of nanoparticles rise thermal properties of parent liquid and then raise its temperature. Effect of thermal radiation parameter N on temperature profile is exhibited in Fig. 4b. By increasing N raises temperature profile because thermal radiation generates a flow of thermal energy in zone and heat flux at the surface upsurgs, resulting in temperature profile increases. Additionally, hybrid nanofluid has more temperature than nanofluid. The effect of temperature ratio θ_r on temperature profile is seen in Fig. 4c. Profile of temperature appears an increasing function with respect to θ_r . Physically, θ_r values between ambient and surface temperatures are rising for hybrid nanofluid/nanofluid flow, the surface temperature is greater. As a result, $\theta(\eta)$ becomes more intense. The temperature of hybrid nanofluid is found to be higher than nanofluid by increasing θ_r . Fig. 4d depicts the sway of heat generation parameter Q on the temperature profile. Rising values of Q create significant amounts of heat in the flow. Hence, temperature enhances. It is shown that temperature for hybrid nanofluid is larger than nanofluid by changing Q . Fig. 4e explains the Hartmann number M effects on the temperature profile. Raising M improves the temperature profile. Because of a magnetic field, the Lorentz force is produced, which causes some additional heat to be created in the flow. Therefore, rises thermal boundary layer. Furthermore, hybrid nanofluid has higher temperature than nanofluid. Fig. 4f demonstrates Eckert number Ec effect on the temperature profile. Eckert number illustrates the influence of viscous forces on heat transfer. The temperature rises as viscous dissipative heat increases. This happens because Ec derives from kinetic energy of the flow and heat enthalpy difference, so enhance in Ec upsurgs kinetic energy. Thus, increment of Ec rises temperature or potential energy. Furthermore, nanofluid (SWCNTs-water) has a lower temperature than hybrid nanofluid (SWCNTs-MWCNTs/water).

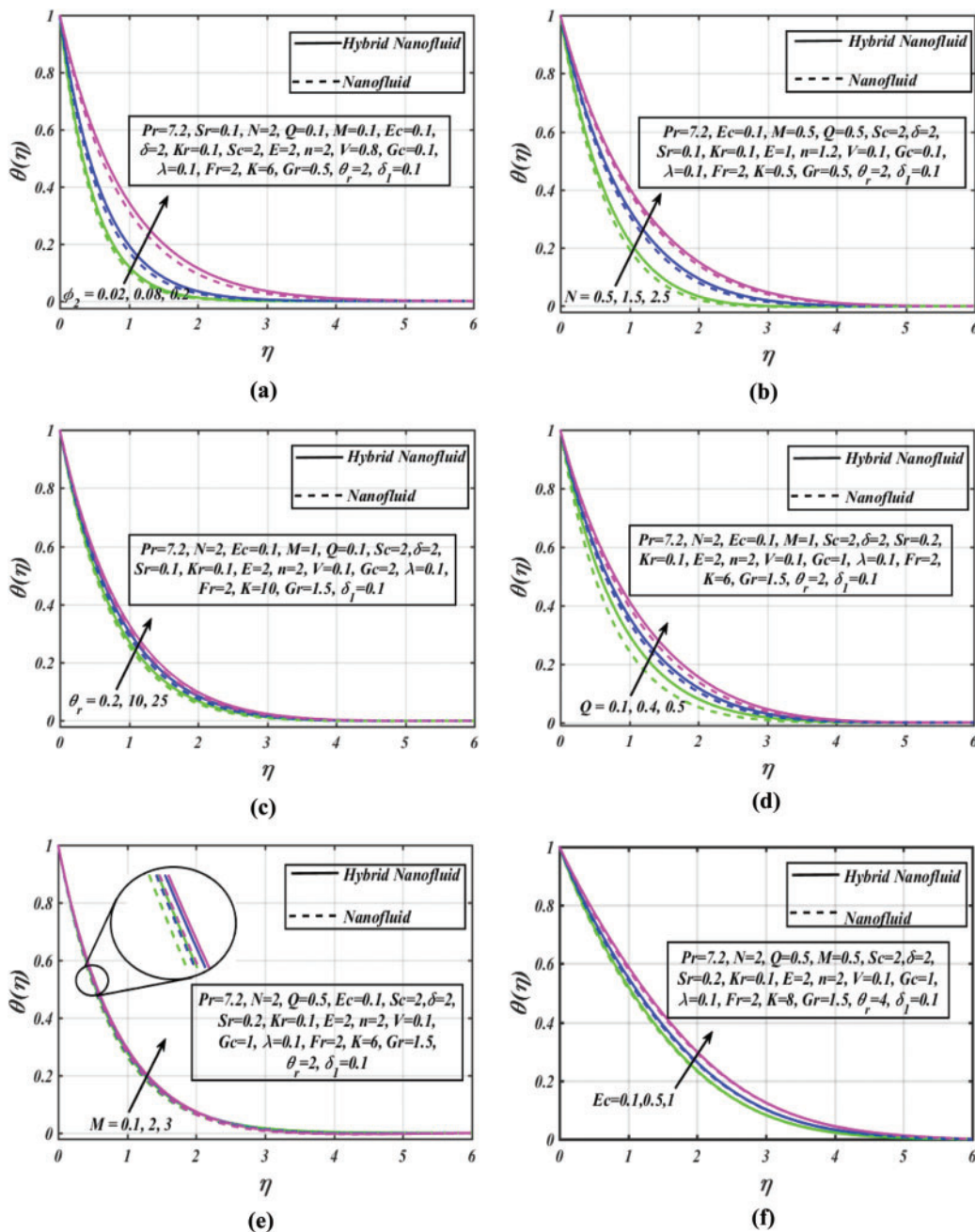


Figure 4: (a) Temperature profile vs. several ϕ_2 values. (b) Temperature profile vs. several N values. (c) Temperature profile vs. several θ_r values. (d) Temperature profile vs. several Q values. (e) Temperature profile vs. several M values. (f) Temperature profile vs. several Ec values

The next contention towards the sway of included parameters on the concentration profile, is presented in Figs. 5a–5g. Fig. 5a demonstrates the effect of volume fraction ϕ_2 towards the concentration profile. The concentration profile lessens by rising ϕ_2 . The reason behind this trend is the fact that an increase in ϕ_2 lead to enhance fluid temperature and thus hot particles collide and move at a faster

rate leading to a decrease in the concentration of solute particles. Furthermore, nanofluid (SWCNTs-water) has a stronger concentration distribution than hybrid nanofluid (SWCNTs-MWCNTs/water). Schmidt number Sc effect on concentration profile is shown in Fig. 5b. The momentum to mass diffusion ratio is called the Schmidt number Sc . Momentum diffusion gives way to mass diffusion, which drops the concentration profile by raising Sc . The magnitude of the concentration profile for nanofluid is discovered to be greater than that of hybrid nanofluid. Fig. 5c shows the chemical reaction parameter Kr effect on concentration distribution. The concentration field decreases by increasing the Kr . This is because of the high rate of chemical reactions, which causes the solute boundary layer to thicken. Moreover, the concentration profile of hybrid nanofluid is lower than nanofluid. Fig. 5d explains the impact of the Soret number Sr towards concentration distribution. Since the ratio of temperature to concentration difference is the Soret number. Greater Sr indicates a larger temperature difference and higher gradient, implying that increasing Sr enhanced concentration distribution of nanoparticles. Moreover, the concentration profile for nanofluid is higher than hybrid nanofluid. Fig. 5e demonstrates the effect of the temperature ratio parameter θ_r on concentration. Raising θ_r reduces concentration profile thus decreasing concentration boundary layer thickness because of a rise in temperature gradient. Hybrid nanofluid (SWCNTs-MWCNTs/water) has a greater concentration profile than nanofluid (SWCNTs-water). Fig. 5f illustrates that the activation energy parameter E impact on the concentration profile. Concentration profile and E have a direct relation. Physically, rate of chemical reaction increases as E increases, and as a result concentration profile $\alpha(\eta)$ is highlighted. Furthermore, it is observed that nanofluid has higher in magnitude than hybrid nanofluid. Fig. 5g explains the influence of the concentration slip parameter δ_1 towards the concentration profile. The sketch clearly shows the concentration profile and δ_1 have an inverse relation across the boundary layer region. Because the liquid particles possessing flow behavior were affected by the solid boundary, which causes the concentration boundary layer to be thin. Furthermore, nanofluid (SWCNTs-water) has a significantly higher concentration profile than hybrid nanofluid (SWCNTs-MWCNTs/water).

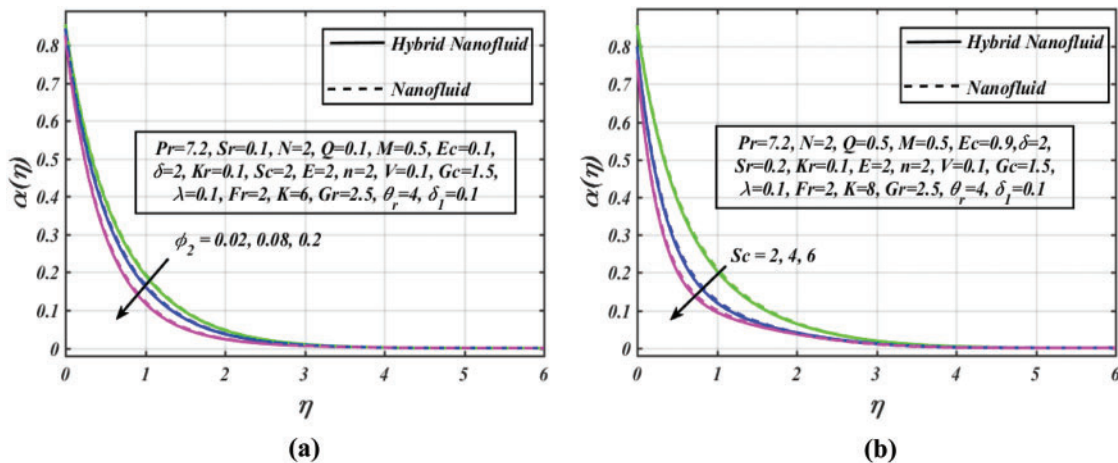


Figure 5: (Continued)

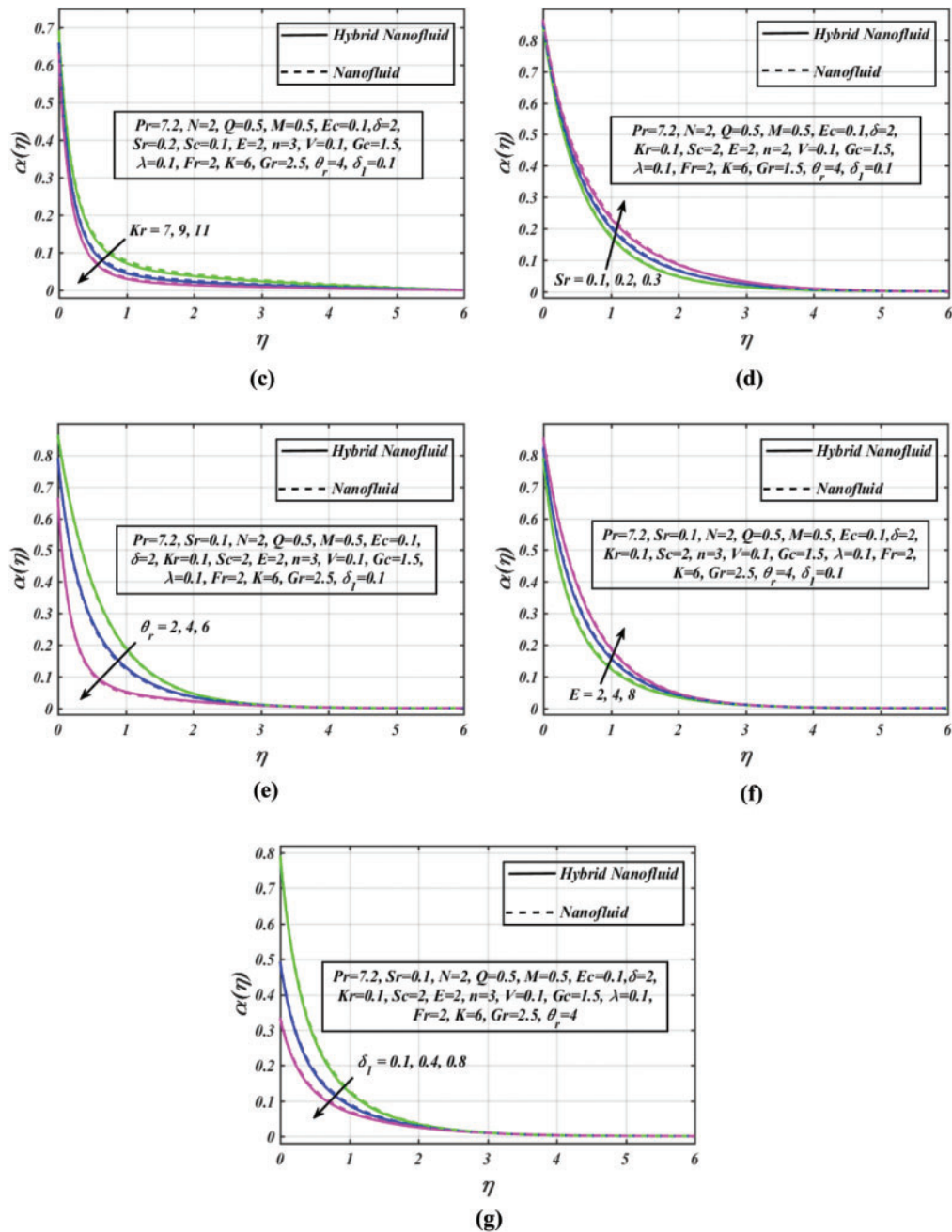


Figure 5: (a) Concentration profile vs. several ϕ_2 values. (b) Concentration profile vs. several Sc values. (c) Concentration profile vs. several Kr values. (d) Concentration profile vs. several Sr values. (e) Concentration profile vs. several θ_r values. (f) Concentration profile vs. several E values. (g) Concentration profile vs. several δ_1 values

Figs. 6–8 provide values for local skin friction coefficient, Nusselt number, and Sherwood number vs. a variety of fluid flow parameters using a bar chart. The impact of K , Fr , δ and V on $C_f\sqrt{Re_x}$ for nanofluid and hybrid nanofluid are displayed through bar chart, see Figs. 6a–6b. Figs. 6c–6d show

the bar chart illustration for numerical values of $C_f\sqrt{Re_x}$ against M , Gr and Gc . It is clearly noticed that porosity parameter, concentration Grashof number and suction parameter enhanced skin friction while Hartmann number, Forchheimer number, thermal Grashof number and velocity slip parameter has a reverse effect on it. Furthermore, against the same parameters, nanofluid (SWCNTs-water) has smaller values of skin friction coefficient than hybrid nanofluid (SWCNTs-MWCNTs/water).

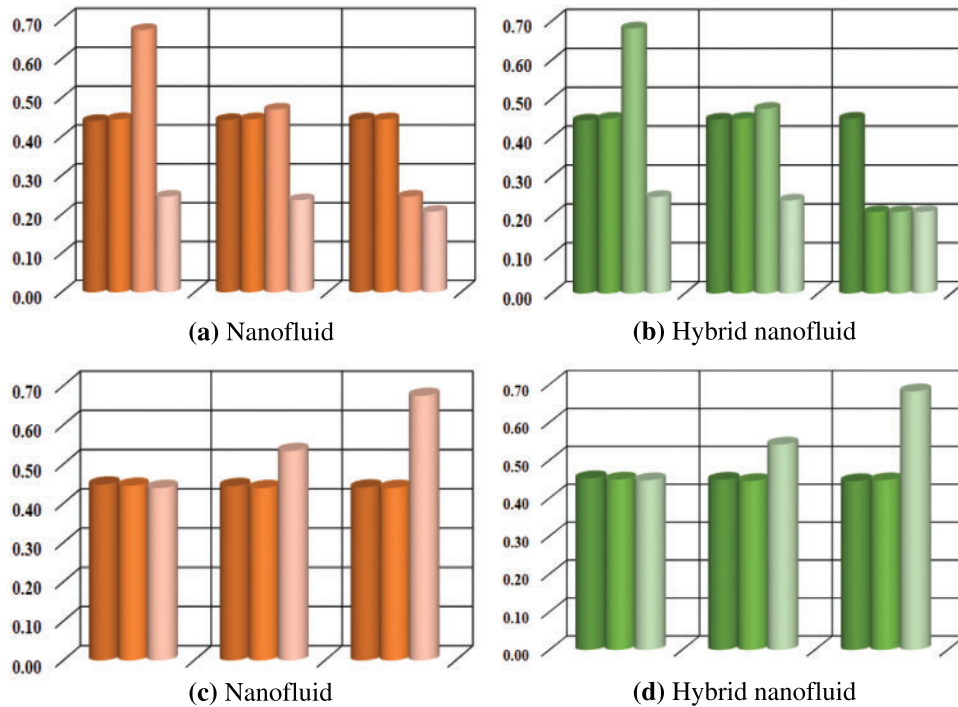


Figure 6: (a–b) Bar chart representation of $C_f\sqrt{Re_x}$ against K , Fr , δ and V . (c–d) Bar chart representation of $C_f\sqrt{Re_x}$ against M , Gr and Gc

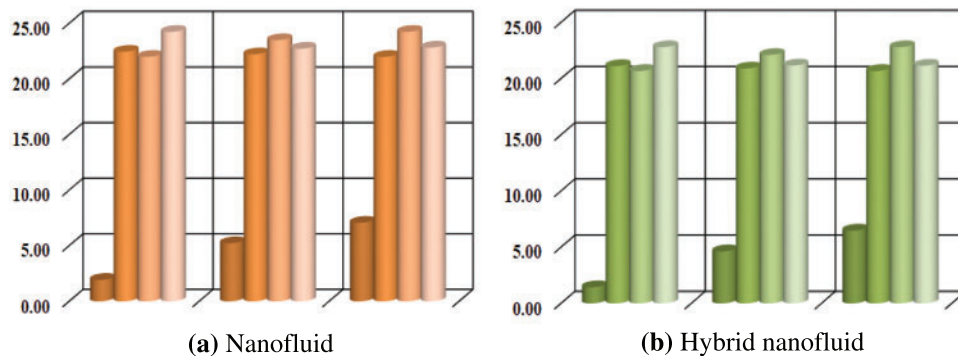


Figure 7: (a–b) Bar chart representation of $Nu_x Re_x^{-1/2}$ against N , Ec , M and Q

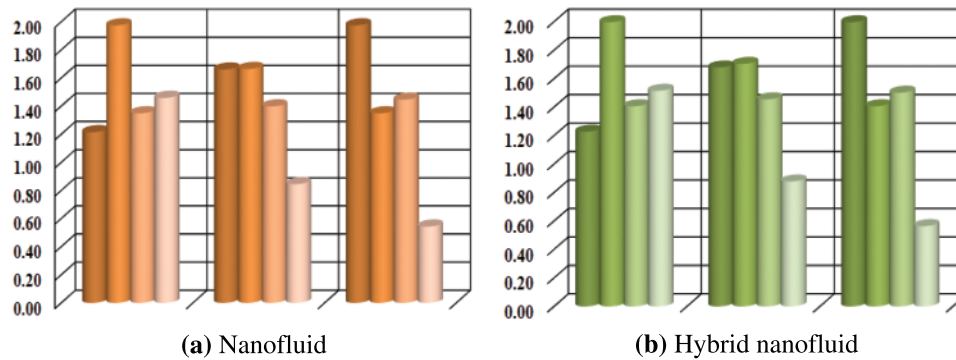


Figure 8: (a–b) Bar chart representation of $Sh_x Re_x^{-1/2}$ against Sc , Sr , Kr and δ_1

Figs. 7a–7b provide the bar chart distribution of $Nu_x Re_x^{-1/2}$ results for hybrid nanofluid and nanofluid against N , Ec , M and Q . M and N are seen to improve the values of Nusselt number. However, Ec and Q have the opposite response. However, when the Nusselt number grows, more heat is transported from the surface to its surroundings, which helps the system to cool. Furthermore, by rising the Eckert number and heat generation parameter the Nusselt number decreases obviously, since both parameters increase enthalpy difference across a thermal boundary layer. Moreover, nanofluid has a greater heat transfer rate than hybrid nanofluid. Figs. 8a–8b determine the bar chart variation of $Sh_x Re_x^{-1/2}$ for both hybrid nanofluid and nanofluid for operating variables like Sc , Sr , Kr and δ_1 . The parameters Sc and Kr are increasing the mass transfer rate while Sr and δ_1 are decreased it. Furthermore, the mass transfer rate for nanofluid (SWCNTs-water) is lesser than hybrid nanofluid (SWCNTs-MWCNTs/water).

5 Concluding Remarks

The present comprehensive numerical study on heat and mass transfer CNTs hybrid fluid flow over a porous surface with the presence of an external magnetic field led to the following notable findings:

- Darcy-Forchheimer parameter contributes to fluid flow deceleration. Moreover, this deceleration is significantly less in the case of CNTs hybrid nanofluid.
- Hartmann number, thermal radiation, heat generation, Eckert number, and temperature ratio parameters show an increasing trend for temperature profile. The temperature of fluid for hybrid nanofluid is higher than nanofluid.
- The Joule heating effect and viscous dissipation lead to an upsurge in fluid temperature and the rise in temperature distribution is prominently more in the presence of hybrid nanofluid. Thus, we conclude that the use of CNTs is more efficient than the utilization of hybrid CNTs.
- Activation energy contributes significantly to enhancing solute particles concentration. Furthermore, we identified that nanofluid has a greater concentration profile than hybrid nanofluid, but the temperature ratio parameter has reversed impact.

Acknowledgement: The authors would like to thank Prince Sultan University for their support through the TAS Research Lab.

Funding Statement: The authors received no specific funding for this study.

Availability of Data and Materials: Not applicable.

Conflicts of Interest: The authors declare that they have no conflicts of interest to report regarding the present study.

References

1. Choi, S. U., Eastman, J. A. (1995). *Enhancing thermal conductivity of fluids with nanoparticles (No. ANL/MSD/CP-84938; CONF-951135-29)*. Argonne, IL (USA): Argonne National Lab (ANL).
2. Ibrahim, W., Shankar, B. (2013). MHD boundary layer flow and heat transfer of a nanofluid past a permeable stretching sheet with velocity, thermal and solutal slip boundary conditions. *Computers & Fluids*, 75, 1–10.
3. Maraj, E. N., Bibi, A., Ijaz, S., Mehmood, R. (2022). MHD carbon nanotubes gravity driven flow along a thermal sensitive porous surface. *Arabian Journal for Science and Engineering*, 1–11. <https://doi.org/10.1007/s13369-022-06775-9>
4. Rekha, M. B., Sarris, I. E., Madhukesh, J. K., Raghunatha, K. R., Prasannakumara, B. C. (2022). Activation energy impact on flow of AA7072-AA7075/water-based hybrid nanofluid through a cone, wedge and plate. *Micromachines*, 13(2), 302.
5. Liu, M. S., Lin, M. C. C., Huang, I. T., Wang, C. C. (2005). Enhancement of thermal conductivity with carbon nanotube for nanofluids. *International Communications in Heat and Mass Transfer*, 32(9), 1202–1210.
6. Maré, T., Halelfadl, S., Sow, O., Estellé, P., Duret, S. et al. (2011). Comparison of the thermal performances of two nanofluids at low temperature in a plate heat exchanger. *Experimental Thermal and Fluid Science*, 35(8), 1535–1543.
7. Shanmugapriya, M., Sundareswaran, R., Senthil Kumar, P. (2021). Heat and mass transfer enhancement of MHD hybrid nanofluid flow in the presence of activation energy. *International Journal of Chemical Engineering*, 2021, 1–12.
8. Kumar, V., Madhukesh, J. K., Jyothi, A. M., Prasannakumara, B. C., Khan, M. I. et al. (2021). Analysis of single and multi-wall carbon nanotubes (SWCNT/MWCNT) in the flow of Maxwell nanofluid with the impact of magnetic dipole. *Computational and Theoretical Chemistry*, 1200, 113223.
9. Ali, M. R., Sadat, R. (2021). Lie symmetry analysis, new group invariant for the (3 + 1)-dimensional and variable coefficients for liquids with gas bubbles models. *Chinese Journal of Physics*, 71, 539–547.
10. Ali, M. R., Sadat, R. (2021). Construction of lump and optical solitons solutions for (3 + 1) model for the propagation of nonlinear dispersive waves in inhomogeneous media. *Optical and Quantum Electronics*, 53(6), 279.
11. Dul, S., Gutierrez, B. J. A., Pegoretti, A., Alvarez-Quintana, J., Fambri, L. (2022). 3D printing of ABS nanocomposites. Comparison of processing and effects of multi-wall and single-wall carbon nanotubes on thermal, mechanical and electrical properties. *Journal of Materials Science & Technology*, 121, 52–66.
12. Wang, Y., Mansir, I. B., Al-Khaled, K., Raza, A., Khan, S. U. et al. (2022). Thermal outcomes for blood-based carbon nanotubes (SWCNT and MWCNTs) with Newtonian heating by using new Prabhakar fractional derivative simulations. *Case Studies in Thermal Engineering*, 32, 101904.
13. Forchheimer, P. (1901). Wasserbewegung durch boden. *Zeitschrift des Vereins Deutscher Ingenieure*, 45, 1782–1788.
14. Muskat, M. (1946). *The flow of homogeneous fluids through porous media*. Ann Arbor, Michigan: JW Edwards. Inc.

15. Sajid, T., Sagheer, M., Hussain, S., Bilal, M. (2018). Darcy-Forchheimer flow of Maxwell nanofluid flow with nonlinear thermal radiation and activation energy. *AIP Advances*, 8(3), 035102.
16. Khan, S. A., Khan, M. I., Hayat, T., Alsaedi, A. (2020). Darcy-Forchheimer hybrid (MoS_2 , SiO_2) nanofluid flow with entropy generation. *Computer Methods and Programs in Biomedicine*, 185, 105152.
17. Yusuf, T. A., Mabood, F., Khan, W. A., Gbadeyan, J. A. (2020). Irreversibility analysis of $\text{Cu-TiO}_2\text{-H}_2\text{O}$ hybrid-nanofluid impinging on a 3-D stretching sheet in a porous medium with nonlinear radiation: Darcy-Forchheimer's model. *Alexandria Engineering Journal*, 59(6), 5247–5261.
18. Gautam, A. K., Verma, A. K., Bhattacharyya, K., Mukhopadhyay, S., Chamkha, A. J. (2021). Impacts of activation energy and binary chemical reaction on MHD flow of Williamson nanofluid in Darcy-Forchheimer porous medium: A case of expanding sheet of variable thickness. *Waves in Random and Complex Media*, 31, 1–22.
19. Raja, M. A. Z., Shoaib, M., Zubair, G., Khan, M. I., Ahmad, S. et al. (2022). Neural artificial networking for a nonlinear Darcy-Forchheimer chemically reactive flow: Levenberg marquardt analysis. *Modern Physics Letters B*, 36(20), 2250095.
20. Joshi, N., Upreti, H., Pandey, A. K. (2022). MHD Darcy-Forchheimer $\text{Cu-Ag/H}_2\text{O-C}_2\text{H}_6\text{O}_2$ hybrid nanofluid flow via a porous stretching sheet with suction/blowing and viscous dissipation. *International Journal for Computational Methods in Engineering Science and Mechanics*, 23(6), 527–535.
21. Alshehri, A., Shah, Z. (2022). Computational analysis of viscous dissipation and Darcy-Forchheimer porous medium on radioactive hybrid nanofluid. *Case Studies in Thermal Engineering*, 30, 101728.
22. Mabood, F., Berrehal, H., Yusuf, T. A., Khan, W. A. (2022). Carbon nanotubes-water between stretchable rotating disks with convective boundary conditions: Darcy-Forchheimer scheme. *International Journal of Ambient Energy*, 43(1), 3981–3994.
23. Bestman, A. R. (1990). Natural convection boundary layer with suction and mass transfer in a porous medium. *International Journal of Energy Research*, 14(4), 389–396.
24. Khan, M. I., Qayyum, S., Hayat, T., Waqas, M., Khan, M. I. et al. (2018). Entropy generation minimization and binary chemical reaction with arrhenius activation energy in MHD radiative flow of nanomaterial. *Journal of Molecular Liquids*, 259, 274–283.
25. Ahmad, S., Nadeem, S. (2020). Analysis of activation energy and its impact on hybrid nanofluid in the presence of hall and ion slip currents. *Applied Nanoscience*, 10, 5315–5330.
26. Khan, N. S., Kumam, P., Thounthong, P. (2020). Second law analysis with effects of arrhenius activation energy and binary chemical reaction on nanofluid flow. *Scientific Reports*, 10(1), 1–16.
27. Maraj, E. N., Khatoon, Z., Ijaz, S., Mehmood, R. (2021). Effect of arrhenius activation energy and medium porosity on mixed convective diluted ethylene glycol nanofluid flow towards a curved stretching surface. *International Communications in Heat and Mass Transfer*, 129, 105691.
28. Raza, Q., Qureshi, M. Z. A., Khan, B. A., Kadhim Hussein, A., Ali, B. et al. (2022). Insight into dynamic of mono and hybrid nanofluids subject to binary chemical reaction, activation energy, and magnetic field through the porous surfaces. *Mathematics*, 10(16), 3013.
29. Maxwell, J. C. (1873). *A treatise on electricity and magnetism*, vol. 1. Oxford: Clarendon Press.
30. Brinkman, H. C. (1952). The viscosity of concentrated suspensions and solutions. *The Journal of Chemical Physics*, 20(4), 571.
31. Xuan, Y., Li, Q., Hu, W. (2003). Aggregation structure and thermal conductivity of nanofluids. *AIChE Journal*, 49(4), 1038–1043.
32. Hayat, T., Hussain, Z., Alsaedi, A., Mustafa, M. (2017). Nanofluid flow through a porous space with convective conditions and heterogeneous-homogeneous reactions. *Journal of the Taiwan Institute of Chemical Engineers*, 70, 119–126.

33. Nandi, S., Kumbhakar, B., Seth, G. S., Chamkha, A. J. (2021). Features of 3D magneto-convective nonlinear radiative Williamson nanofluid flow with activation energy, multiple slips and hall effect. *Physica Scripta*, 96(6), 065206.
34. Nandi, S., Kumbhakar, B., Sarkar, S. (2022). MHD stagnation point flow of $\text{Fe}_3\text{O}_4/\text{Cu}/\text{Ag}-\text{CH}_3\text{OH}$ nanofluid along a convectively heated stretching sheet with partial slip and activation energy: Numerical and statistical approach. *International Communications in Heat and Mass Transfer*, 130, 105791.
35. Wang, C. Y. (2002). Flow due to a stretching boundary with partial slip—An exact solution of the Navier–Stokes equations. *Chemical Engineering Science*, 57(17), 3745–3747.
36. Noghrehabadi, A., Saffarian, M. R., Pourrajab, R., Ghalambaz, M. (2013). Entropy analysis for nanofluid flow over a stretching sheet in the presence of heat generation/absorption and partial slip. *Journal of Mechanical Science and Technology*, 27, 927–937.